

PAPER

[View Article Online](#)
[View Journal](#) | [View Issue](#)Cite this: *Mater. Adv.*, 2022,
3, 4736Synthesis of SrTiO₃ and Al-doped SrTiO₃ via the deep eutectic solvent route†Adedoyin N. Adeyemi,^a Amrit Venkatesh,^{ab} Chengcan Xiao,^c Zeqiong Zhao,^c Ying Li,^a Tori Cox,^a Dapeng Jing,^{bd} Aaron J. Rossini,^{ab} Frank E. Osterloh,^c and Julia V. Zaikina^{id}*^a

SrTiO₃ and aluminum-doped SrTiO₃ are synthesized by calcination of metal salts dissolved in a deep eutectic solvent (DES) without any post-synthesis treatment. The DES used is the eutectic mixture of choline chloride (hydrogen bond acceptor) and malonic acid (hydrogen bond donor). Titanium(IV) oxide bis(2,4-pentanedionate) is utilized as the non-volatile, easy-to-handle, DES-soluble titanium precursor. The ammonia gas evolved during the calcination process provides a reducing atmosphere, resulting in the formation of Ti³⁺ and oxygen vacancies within the SrTiO₃ matrix. According to UV-Vis spectroscopy and X-ray photoelectron spectroscopy, the amount of Ti³⁺ species and oxygen vacancies (V_O) in the synthesized perovskite can be tuned by varying the duration of the calcination process and by adding Al³⁺ dopants. Solid state ²⁷Al NMR spectroscopy and powder X-ray diffraction confirm the doping of aluminum into the octahedral site of the perovskite structure. Surface photovoltage spectroscopy confirms that Al³⁺ dopants can eliminate Ti³⁺ defects in Al-doped SrTiO₃. Ultraviolet illumination experiments in water and aqueous methanol show that SrTiO₃ and aluminum-doped SrTiO₃, after modification with Rh_xCr_{2-x}O₃ or Pt co-catalysts, evolve small amounts of H₂ (EQE of 0.0113–0.0173% at 375 nm) with only traces of O₂ detected. The lack of photocatalytic activity is attributed to rapid electron-hole recombination in the oxygen vacancy-rich materials and to the lack of crystal facets that could aid charge separation.

Received 8th April 2022,
Accepted 3rd May 2022

DOI: 10.1039/d2ma00404f

rsc.li/materials-advances

Introduction

Deep eutectic solvents (DESS) are analogs of ionic liquids (ILs).^{1–3} Unlike conventional ILs, which are made up of discrete ions, DESS are made of a hydrogen bond acceptor (usually quaternary ammonium halides) and a hydrogen bond donor, thus DESS possess both hydrogen bonding and ionic interactions. The majority of DESS utilize 2-hydroxyethyltrimethylammonium chloride (choline chloride) as the hydrogen bond acceptor combined with a hydrogen bond donor such as urea, oxalic acid, citric acid, or acetamide, *etc.*^{2,4} When these two solids are mixed, they form a low melting eutectic mixture, that is a liquid at room temperature.¹ DESS are non-toxic and biodegradable solvents; they have low melting points and are environmentally friendly.⁵ Owing to the high solubility of selected

binary oxide or metal precursors in DESS,³ they are attractive replacements for corrosive inorganic acids as a reaction medium in solution synthesis of materials.³ Several ternary oxides such as spinel-type ferrite nanoparticles,⁶ zinc and copper vanadates like M₂V₂O₇ and MV₂O₆ (M = Zn or Cu),^{7,8} and barium titanate BaTiO₃⁹ have been previously synthesized using the DES route. Except for BaTiO₃, these ternary oxides were synthesized by dissolving binary metal oxides in DESS, followed by calcination of the resulting solution in air at 500 °C or higher temperatures. BaTiO₃ was synthesized from barium acetate and titanium isopropoxide,⁹ because unlike many other binary oxides, TiO₂ is insoluble in any of the studied DESS.³

Strontium titanate, SrTiO₃ is a functional oxide often used as a dielectric material^{10–12} and has been recently investigated for thermoelectric applications.^{13,14} It is also a semiconductor with reported bandgaps in the range of 3.0 eV to 3.88 eV.^{15–18} Due to the size of the band gap and the position of the valence/conduction band edge, strontium titanate, is a suitable catalyst for overall photocatalytic water splitting.^{19,20}

SrTiO₃ exists as an intrinsic non-stoichiometric compound which contains two types of defects: oxygen vacancies and Ti³⁺ species. When the Ti–O bond breaks, O₂ gas is released to yield oxygen vacancies as well as free electrons, which reduce Ti⁴⁺

^a Department of Chemistry, Iowa State University, Ames, Iowa 50011, USA.E-mail: yzaikina@iastate.edu^b Ames Laboratory, US DOE, Iowa State University, Ames, Iowa 50011, USA^c Department of Chemistry, University of California at Davis, Davis, California 95616, USA^d Materials Analysis and Research Laboratory, Iowa State University, Ames, IA 50011, USA† Electronic supplementary information (ESI) available. See DOI: <https://doi.org/10.1039/d2ma00404f>

Mater. Adv., 2022, **3**, 4736–4747 | 4737

energy of 150 eV were energy analysed using a DuPont analyser. Raw data files were processed using CasaXPS, and a Shirley baseline was applied to all spectra.

Scanning electron microscopy (SEM) and energy dispersive X-ray spectroscopy (EDXS). The morphology of the synthesized samples was inspected using SEM utilizing an FEI Quanta 250 field emission scanning electron microscope at 15 kV. EDXS was performed using Oxfords X-Max 80 detector for elemental composition analysis. Powdered samples were deposited on a SEM sample holder using carbon tape. The samples were coated with 5 nm of iridium metal.

Solid-state NMR spectroscopy. ^{27}Al solid-state NMR was carried out on all the samples using a Bruker widebore 9.4 T (400 MHz) NMR spectrometer equipped with an Avance III HD console. Spectra were acquired using a 2.5 mm triple-resonance (HXY) MAS probe. The MAS rate was 25 kHz in all cases. A standard pulse-acquire method with a ^{27}Al pulse duration of 0.3 μs corresponding to an 8° tip angle (*ca.* 75 kHz rf field) was used to obtain quantitative ^{27}Al solid-state NMR spectra.^{39,40} Spectra were processed using the Bruker Topspin package; deconvolution of the different ^{27}Al signals and fitting to Cjzjek distribution⁴¹ was performed using the ssNake program.⁴²

Surface photovoltage (SPV) spectroscopy. SPV spectroscopy was performed on particle films on fluorine-doped tin oxide (FTO) substrates. These films were prepared by drop coating aqueous SrTiO_3 and Al-doped SrTiO_3 suspensions (5 mg mL^{-1}) onto the FTO, followed by annealing at 300 $^\circ\text{C}$ for 2 h in air. SPV measurements were done under vacuum (1×10^{-4} mbar) with a vibrating gold mesh Kelvin probe (Besocke Delta phi). Monochromatic light used as the irradiation source was produced by a 150 W Xe lamp and an Oriel Cornerstone 130 monochromator. The light intensity at the sample surface is 1–3 mW cm^{-2} . Spectra were acquired by stepping the photon energy by 0.0124 eV every 5 s and by measuring the contact potential difference (CPD) value at each step. All CPD values in Fig. 11 are reported relative to the CPD value in the dark. Positive values correspond to electrons moving toward the Kelvin probe and negative values correspond to electrons moving away from the Kelvin probe. Additional details can be found elsewhere.⁴³

Deposition of the cocatalysts. $\text{Rh}_x\text{Cr}_{2-x}\text{O}_3$ cocatalyst was loaded onto the surface of SrTiO_3 or $\text{SrTiO}_3:\text{Al}$ particles with a weight ratio of $\text{Rh}:\text{Cr}:\text{SrTiO}_3$ (or $\text{SrTiO}_3:\text{Al}$) = 1:1:1000, as described previously.⁴⁴ Typically, 150 mg SrTiO_3 or $\text{SrTiO}_3:\text{Al}$ was mixed with appropriate amount of RhCl_3 and $\text{Cr}(\text{NO}_3)_3$ solutions containing 0.15 mg Rh and 0.15 mg Cr in a vial in a 70 $^\circ\text{C}$ water bath, and water was slowly evaporated under constant stirring. The product was then transferred to a furnace and heated at 350 $^\circ\text{C}$ in air for 1 h to produce $\text{Rh}_x\text{Cr}_{2-x}\text{O}_3$ loaded SrTiO_3 or $\text{SrTiO}_3:\text{Al}$ in 95% yield. Pt-modified SrTiO_3 and $\text{SrTi}_{0.9}\text{Al}_{0.1}\text{O}_3$ (heating profile 1) were made by photo-deposition, using 100 mg SrTiO_3 ($\text{SrTiO}_3:\text{Al}$) particles, a H_2PtCl_6 stock solution (2 mg Pt mL^{-1}) and 100 mL 20% of aqueous methanol solution with the weight percentage of Pt to SrTiO_3 (or $\text{SrTiO}_3:\text{Al}$) being 2%. The mixture was sonicated for 10 min and bubbled with N_2 for 10 min, then connected to the online Gas Chromatography system (SRI 8610c) with a 300W Xe

lamp and magnetic stirring. H_2 generation was recorded during photo-deposition to pinpoint the end point of this process. A typical photo-deposition lasts for 4–5 hours until the H_2 generation rate becomes constant. After photo-deposition, the Pt loaded particles were centrifuged and washed with water for 3 times, re-suspended in 20% volume ratio methanol and made ready for hydrogen evolution experiment.

Photocatalytic experiments. The water splitting experiments were conducted in a quartz round bottom flask with a mixture of 100 mg $\text{Rh}_x\text{Cr}_{2-x}\text{O}_3/\text{SrTiO}_3$ (or $\text{Rh}_x\text{Cr}_{2-x}\text{O}_3/\text{SrTiO}_3:\text{Al}$) powder and 100 mL ultra-purified water using Xe-lamp. The suspension was sonicated for 10 min and bubbled with N_2 for 10 min before irradiation to remove any residual O_2 dissolved in it. Then, the flask was connected to the online Gas Chromatography system (SRI 8610c) with a 300W Xe lamp and magnetic stirring. UV intensity was measured to be 100 mW cm^{-2} with a GaN photodetector (SEL 270) connected to an ILT1400 International Light photometer. Hydrogen evolution reaction/External quantum efficiency (EQE) measurements were conducted similarly, using a mixture of 100 mg Pt/ SrTiO_3 or Pt/ $\text{SrTiO}_3:\text{Al}$ in 118 mL of 20% aqueous methanol solution. The quartz flask was covered with aluminum foil leaving only a 1.531 cm^2 window for incident light from the 375 nm LED. The LED light intensity was measured with a SEL623 Thermopile detector connected to an ILT1400 International Light photometer. Details of EQE calculation are given in the Supporting Information.

Results and discussion

The DES employed in this synthesis was choline chloride-malonic acid mixed in a 1:1 molar ratio. TiO_2 is not soluble in any studied DES, but titanium isopropoxide has previously been utilized for the synthesis of BaTiO_3 using a DES.⁹ However, both titanium isopropoxide and titanium(IV) chloride are flammable fuming liquids which readily undergoes hydrolysis upon contact with humid air, making them unpleasant precursors to work with. Here we utilized titanium(IV) oxide bis(2,4-pentanedionate)(TOPD)⁴⁵ as a DES-soluble precursor. TOPD, which is the source of titanium in this synthesis dissolves in the choline chloride-malonic acid DES to give a yellow viscous solution in a parafilm covered beaker. When a laser beam (from a laser pointer) is passed through the yellow viscous solution (Fig. 1(a)), no Tyndall scattering was observed, confirming that that TOPD indeed formed a true solution in DES, not just a dispersion of colloidal particles. TOPD is a more convenient precursor to use since it is a powder (thus easy to weigh) and it does not produce fumes unlike other typically used Ti precursors.

The resulting yellow stable viscous solution was transferred into an open porcelain crucible and calcined in air, removing the organic solvent. The organic components are combusted below or at 500 $^\circ\text{C}$. Ammonia, hydrogen chloride, carbon dioxide and water are evolved as gaseous by-products. Powder X-ray diffraction (PXRD) patterns were collected *ex situ* at



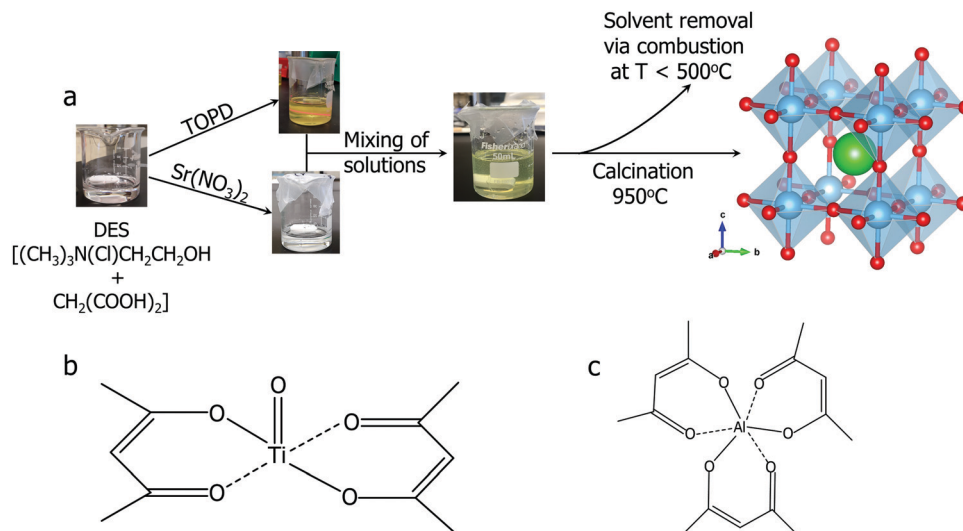


Fig. 1 (a) Synthetic route of strontium titanate SrTiO₃. Atom color coding used: Sr (green), Ti (blue), O (red); (b) molecular structure of titanium(IV) oxide bis(2,4-pentanedionate) (TOPD); (c) molecular structure of aluminum 2,4-pentanedionate.

different calcination temperatures to monitor the progress of the reaction (Fig. 2). During the calcination of the transparent, yellow viscous solution, the sample remains amorphous up to 300 °C.

The first set of peaks appearing at 400 °C correspond to two phases: strontium chloride dihydrate (SrCl₂·2H₂O) and anatase TiO₂. Peaks of cubic SrTiO₃ (perovskite structure, *Pm*3̄*m*) begin to appear at 600 °C with SrCl₂·2H₂O and anatase TiO₂ still present. As the peaks of SrTiO₃ become more intense, the intensity of SrCl₂·2H₂O peaks decrease. At 950 °C the reaction is complete, and SrTiO₃ is the primary product with a minor impurity of both anatase and rutile TiO₂ (5 wt%), as determined by Rietveld refinement of PXRD data. Overall, SrCl₂·2H₂O and

TiO₂ formed first, and further reaction occurs upon an increase in temperature to yield SrTiO₃. The result of this stepwise calcination process differs from the previously reported synthesis of BaTiO₃,⁹ since the Bragg's peaks corresponding to SrTiO₃ appeared as early as 600 °C whereas peaks corresponding to BaTiO₃ were not observed until 850 °C. Additionally, the DES-assisted synthesis of BaTiO₃ proceeds through a BaCl₂ intermediate while that of SrTiO₃ proceeds through a SrCl₂·2H₂O intermediate. We hypothesize that the difference in the type of the chloride intermediates arises because for BaTiO₃ synthesis, precursors were stirred in an open container at 90 °C until water evaporated. In contrast, our synthesis of SrTiO₃ used stirring in a parafilm covered beaker which discourages evaporation. Since the little amount of water present in the hygroscopic choline chloride is not allowed to evaporate during mixing, this water may lead to the formation of a hydrated chloride intermediate, SrCl₂·2H₂O.

Due to the small concentration of metal precursors in the DES, the yellow viscous solution is very dilute. Two heating profiles are employed for the calcination process: heating profile 1 and heating profile 2. Heating profile 2 is similar to that used in the synthesis of BaTiO₃,⁹ it is a rapid calcination and had an overall shorter dwelling time (see experimental details). It was observed that the primary yield of SrTiO₃ made from both heating profiles is ~91%. The secondary yield, however, is different for samples made *via* different heating profiles. The samples made using heating profile 1 have large clusters, and can be easily transferred from the crucibles, leading to a higher secondary yield of 77% (occasionally, the yield can be as high as 88%). However, samples made by heating profile 2 are mostly sintered to the crucibles. Also, the particles are smaller, unclustered, lightweight, and so are easily lost during the transfer from the crucibles. This leads to a lower secondary yield when heating profile 2 is employed (23%).

The weight percent of impurities present in the synthesized samples was evaluated by Rietveld refinement of PXRD data.

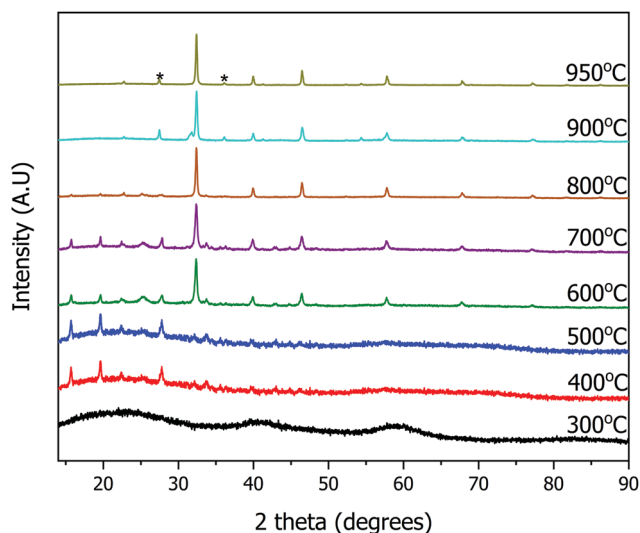


Fig. 2 *Ex situ* powder X-ray diffraction patterns of the calcined sample for the synthesis of SrTiO₃ at various temperatures. TiO₂ impurity peaks are marked with asterisks (*).

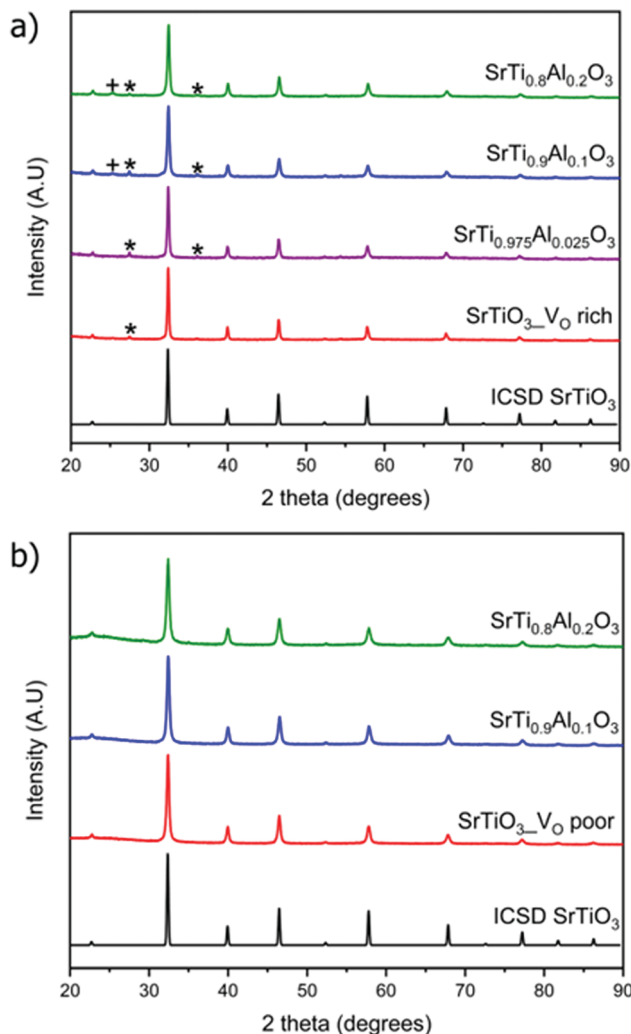


Fig. 3 Powder X-ray diffraction patterns of doped and undoped (a) V_O rich $SrTiO_3$ made with heating profile 1 and (b) V_O poor $SrTiO_3$ made with heating profile 2. Peaks that belong to rutile TiO_2 impurity are marked with asterisks (*) while peaks belonging to anatase TiO_2 impurity are marked with plus sign (+). ICSD 192314 was used for $SrTiO_3$.

Samples made with heating profile 1 contain the cubic $SrTiO_3$ (~ 95 wt%) as well as both rutile TiO_2 and anatase TiO_2 impurity which accounted for 5 wt% of the sample (Fig. 3). The impurity peaks of rutile and anatase TiO_2 were absent in the PXRD pattern of $SrTiO_3$ prepared *via* heating profile 2. We observed that the slower and longer heating profile 1 allowed the formation of TiO_2 impurities as opposed to the shorter and faster heating profile 2. As it was further determined by several characterization methods, the primary difference between $SrTiO_3$ samples produced *via* two heating profiles is the concentration of O vacancies: heating profile 1 resulted in the $SrTiO_3$ that is rich in O vacancies (V_O rich), while heating profile 2 leads to $SrTiO_3$ that is poor in O vacancies (V_O poor). For the sake of clarity, we refer to the samples prepared *via* heating profile 1 as “ V_O rich” and *via* heating profile 2 as “ V_O poor” throughout the text.

Since the doping of $SrTiO_3$ with aluminum has been reported to increase the rate of photocatalytic activity of $SrTiO_3$,^{22–25} aluminum-doped samples $SrTi_{1-x}Al_xO_3$ were synthesized using the same two heating profiles. The maximum loading fraction of Al used was $x = 0.2$ because further increase in Al dopant concentration resulted in a $SrAlO_2$ impurity as evident from PXRD data. The doped samples made with heating profile 1 also have the anatase and rutile TiO_2 impurities. Similar to undoped $SrTiO_3$, these impurities are absent in the doped samples made with heating profile 2 because the faster and shorter heating profile does not favour the formation of TiO_2 impurities (Fig. 3). The replacement of Ti^{4+} (0.605 \AA) in octahedral sites with smaller Al^{3+} (0.535 \AA) is expected to result in the reduction of the cubic unit cell parameters. Rietveld refinement using LaB_6 as an internal standard was carried out to determine the change in unit cell upon Al doping (Fig. 4). The unit cell parameter of V_O rich $SrTi_{1-x}Al_xO_3$ are generally smaller than that V_O poor $SrTi_{1-x}Al_xO_3$ as shown in Fig. 4. As expected, with the increase of Al content, the unit cell parameter decreases until $x = 0.1$, *i.e.*, the unit cell parameter of $SrTi_{0.9}Al_{0.1}O_3$ is very similar to that of $SrTi_{0.8}Al_{0.2}O_3$, suggesting that maximal Al dopant concentration is $x < 0.2$.

The crystallite size of V_O rich samples calculated from the Debye Scherrer equation on average decreases with increase in aluminum doping while the crystallite size of V_O poor samples remain constant regardless of aluminum doping (Table 1).

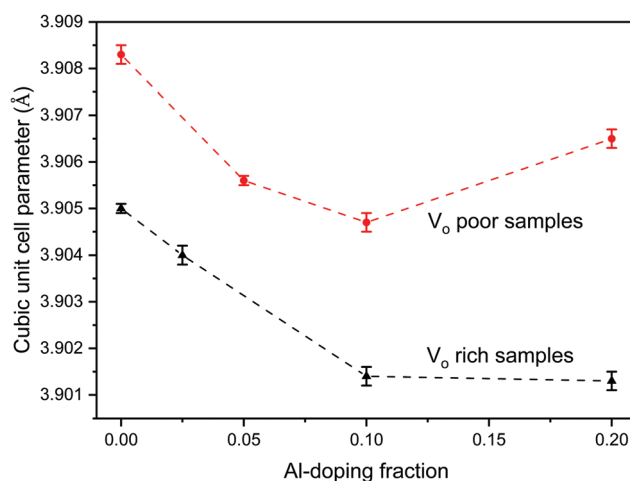


Fig. 4 Change in cubic unit cell parameter of the V_O rich $SrTi_{1-x}Al_xO_3$ made with heating profile 1 (black) and V_O poor $SrTi_{1-x}Al_xO_3$ made with heating profile 2 (red) as a function of Al doping, x .

Table 1 Crystallite sizes of the $SrTi_{1-x}Al_xO_3$ ($x = 0$ to 0.2)

Samples	Crystallite size ^a (nm)	
	Heating 1 (V_O rich)	Heating 2 (V_O poor)
$SrTiO_3$	40 (6)	24(4)
$SrTi_{0.975}Al_{0.025}O_3$	31(5)	NA
$SrTi_{0.95}Al_{0.05}O_3$	27(2)	NA
$SrTi_{0.9}Al_{0.1}O_3$	26(4)	23(3)
$SrTi_{0.8}Al_{0.2}O_3$	21(3)	20(3)

^a Calculated using Debye Scherrer equation.

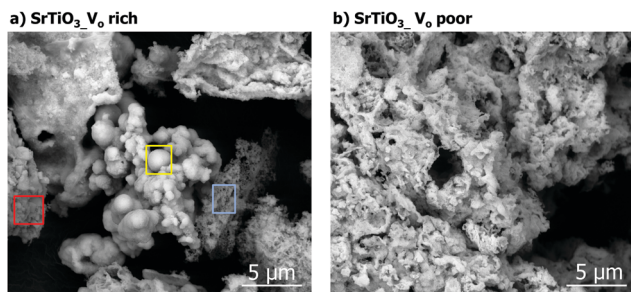


Fig. 5 SEM image of (a) V_O rich $SrTiO_3$ made with heating profile 1 and (b) V_O poor $SrTiO_3$ made with heating profile 2.

Scanning electron microscopy (SEM) images of the samples showed the doped and undoped V_O rich $SrTiO_3$ have structured crystallites (in red, Fig. 5(a)), nanoclusters (in yellow, Fig. 5(a)), and flakes (in blue, Fig. 5(a)). On the contrary, the V_O poor samples all appeared to be in the form of flakes (or sheets), regardless of the presence or absence of aluminum (Fig. 5 and Fig. S1, ESI†). Energy Dispersive X-ray Spectroscopy (EDXS) of Al-doped sample indicates the homogeneous distribution of Sr, Ti and Al in the samples.

^{27}Al solid-state NMR spectroscopy

Aluminum is expected to replace titanium in the octahedral site of the $SrTiO_3$ perovskite structure based on the similarity of ionic radii. ^{27}Al solid-state NMR spectra of the doped samples were obtained to prove doping of aluminum in a symmetric octahedral site in the perovskite structure (Fig. 6). ^{27}Al is a spin-

$5/2$ quadrupolar nucleus with a natural abundance of 100% and a high sensitivity to the coordination environment and symmetry. We note that solid-state NMR spectroscopy has previously been used to extensively characterize $SrTiO_3$ and related perovskite materials.^{46–49} The NMR spectra were fitted to three signals: a broad peak with an isotropic shift (δ_{iso}) of ca. 83 ppm corresponding to a tetrahedral site, a broad signal with δ_{iso} of 16 ppm corresponding to an octahedral site, and a narrow signal with δ_{iso} of 9 ppm that is assigned to the doped octahedral site of the perovskite structure. The broad tetrahedral and octahedral signals are characteristic of alumina,⁵⁰ and were assigned to an amorphous alumina impurity that could not be detected by PXRD.⁴⁹ The tail of the broad ^{27}Al NMR signals at lower chemical shifts is indicative of a distribution of quadrupolar couplings that is intrinsic to amorphous alumina.⁵⁰ The sharp signal at 9 ppm represents a ^{27}Al site with low quadrupolar broadening and must therefore correspond to a site of high spherical symmetry; this observation confirms the aluminum doping into the titanium octahedral site in $SrTiO_3$. To ensure quantitative excitation of the various ^{27}Al signals, a small tip angle pulse was used (see experimental).^{39,40}

Fig. 6(a) compares the ^{27}Al solid-state NMR obtained with different Al doping levels. Note that the intensities are normalized with respect to the sharp ^{27}Al NMR signal at 9 ppm. It is evident that as the Al doping level increases the concentration of the alumina impurity also increases. Next, the spectra were deconvoluted and fit using the Cjzek distribution to model the distribution in quadrupolar couplings of the alumina impurity (Fig. S2, ESI†). The fraction of the octahedral doped ^{27}Al sites in perovskite structure (% doping, Table 2) was then estimated from the absolute integrals of the deconvoluted peaks.

Notably, the actual fraction of aluminum doped into the structure (actual x , Table 2) was lower than the nominal fraction. As the nominal doping fraction increases, so does the actual doping fraction (Fig. 6(b)). However, the percentage of aluminum being doped into the structure decreases as the aluminum doping fraction increases, suggesting that at higher nominal Al fraction more alumina is forming (Table 2).

Diffuse reflectance and bandgap measurement

The diffuse reflectance was measured for all samples and expressed as Tauc plots to calculate the direct band gap (Fig. 7). All the V_O rich samples showed an approximate direct

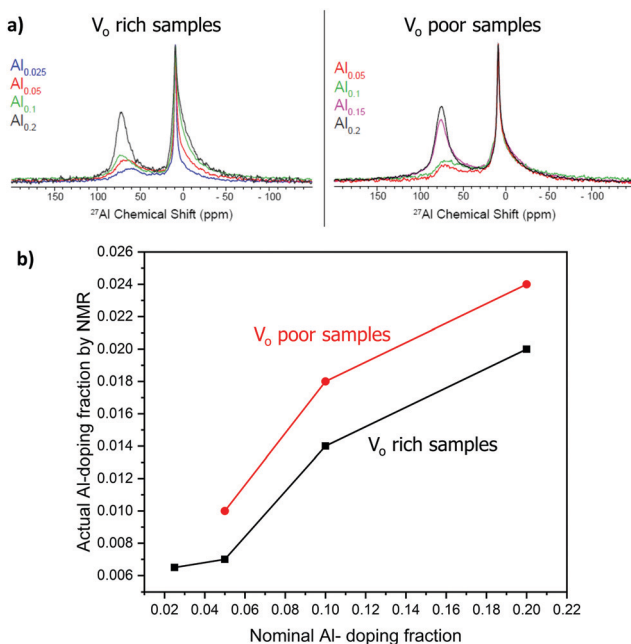


Fig. 6 ^{27}Al solid-state NMR. (a) Comparison of 1D spectra; signal intensities are normalized with respect to the sharp signal at ca. 9 ppm. (b) Plot showing the actual and nominal aluminum doping concentration trend for V_O rich samples made with heating 1 (black curve) and V_O poor samples made heating 2 (red curve).

Table 2 Percent concentration of nominal aluminum actually doping into the structure

Nominal x in $SrTi_{1-x}Al_xO_3$	Heating 1 (V_O rich)		Heating 2 (V_O poor)	
	% Doping ^a	Actual x	% Doping ^a	Actual x
0.025	26	0.0065	NA	NA
0.05	14	0.007	20	0.01
0.1	14	0.014	18	0.018
0.2	10	0.02	12	0.024

^a (Nominal x) \times (% doping) = Actual x .

band gap of 3.0 eV and all V_O poor samples showed an approximate direct band gap of 3.2 eV as shown in Fig. 7 and Fig. S3 (ESI†). The doping of the samples with Al does not significantly affect their bandgaps for either heating profile. Doped and undoped $SrTiO_3$ samples made with heating profiles 1 and 2 showed beige colors but with different intensities. The color of the synthesized samples can be attributed to the presence of oxygen vacancies and high concentration of Ti^{3+} . It has been previously reported that $SrTiO_3$ samples containing a high amount of Ti^{3+} usually possess color,²² in support of our observation.

Both undoped and doped samples made with heating profile 1 were darker beige in color, as shown in Fig. 7(a). A band tail (or an additional absorption edge) was also noticed in their absorption data (Fig. 7(c)). The darker beige color and a band tail suggest that samples made with heating profile 1 have more Ti^{3+} species and oxygen vacancies (V_O rich). This is in agreement with previous reports where the concentration of Ti^{3+} /oxygen vacancies in $SrTiO_3$ was increased by heating the sample in a reducing environment.^{52,53} Similarly, the decomposition of the DES provides a reducing atmosphere during the synthesis which favors the formation of oxygen vacancies as it was previously shown for zinc and copper vanadates.^{7,8}

Samples made with heating profile 2 (V_O poor) showed a lighter beige color and also a slightly wider bandgap (Fig. 7(b)). The absence of a pronounced band tail in the absorbance spectra of samples made with heating profile 2 (Fig. 7(c)) indicates a lower concentration of Ti^{3+} states.⁵¹ Since the same color was observed in undoped sample and doped sample, we presume that the Al^{3+} dopant did not significantly suppress Ti^{3+} states.

X-Ray photoelectron spectroscopy

XPS measurements were carried out on the $SrTiO_3$ samples to quantify the amount of reduced Ti species. Fig. 8 shows Ti 2p core level spectra of $SrTiO_3$ made with both heating profiles. The two titanium peaks shown originate from spin-orbit splitting of Ti 2p_{3/2} and Ti 2p_{1/2}, each peak is a superposition of 3 components corresponding to Ti^{4+} , Ti^{3+} , and Ti^{2+} . Fig. 8(a) shows the titanium species in V_O rich $SrTiO_3$. The doublet in red at 458.7 eV (Ti 2p_{3/2}) and 464.4 eV (Ti 2p_{1/2}) are assigned to Ti^{4+} , the doublet in blue at 457.6 eV (Ti 2p_{3/2}) and 463.0 eV (Ti 2p_{1/2}) are assigned to Ti^{3+} , while the doublet in magenta at 455.4 eV and 461.4 eV are assigned to Ti^{2+} . Based on the relative Ti 2p_{3/2} peak ratios, the V_O rich sample has 73.5% of titanium present as Ti^{3+} , 19.2% as Ti^{4+} , and 7.3% as Ti^{2+} . The large quantity of Ti^{3+} present in oxygen vacancy rich $SrTiO_3$ agrees with the optical properties as discussed above. Fig. 8(b) shows the titanium species in the V_O poor $SrTiO_3$. The doublet in red at 458.5 eV (Ti 2p_{3/2}) and 464.2 eV (Ti 2p_{1/2}) are assigned to Ti^{4+} , the doublet in blue at 457.1 eV (Ti 2p_{3/2}) and 462.9 eV (Ti 2p_{1/2}) are assigned to Ti^{3+} , while the doublet in magenta at 455.3 eV and 461.1 eV are assigned to Ti^{2+} . In contrast to the V_O rich sample, the V_O poor $SrTiO_3$ sample made with heating profile 2 has 72.5% of titanium present as Ti^{4+} , 20.8% as Ti^{3+} and 6.7% as Ti^{2+} . The values of the binding energy of the titanium species

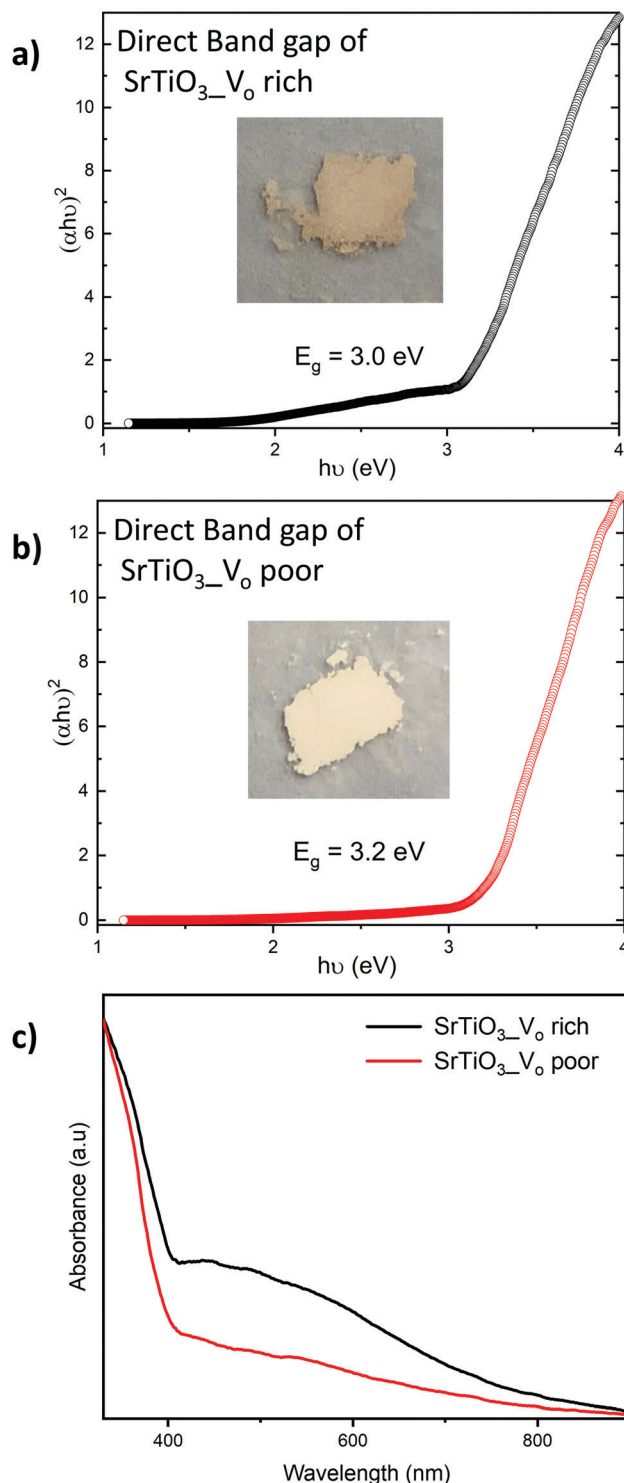


Fig. 7 Tauc plots used to determine direct band gaps of (a) V_O rich $SrTiO_3$ obtained via heating profile 1 and (b) V_O poor $SrTiO_3$ obtained via heating profile 2. Insets show the images of $SrTiO_3$ samples obtained via respective heating profiles. (c) UV-Vis spectra of V_O rich $SrTiO_3$ obtained via heating profile 1 (black curve) and V_O poor $SrTiO_3$ obtained via heating profile 2 (red curve).

observed in this work are similar to those that have previously been reported.^{22,54} The presence of Ti^{3+} and Ti^{2+} in the V_O rich



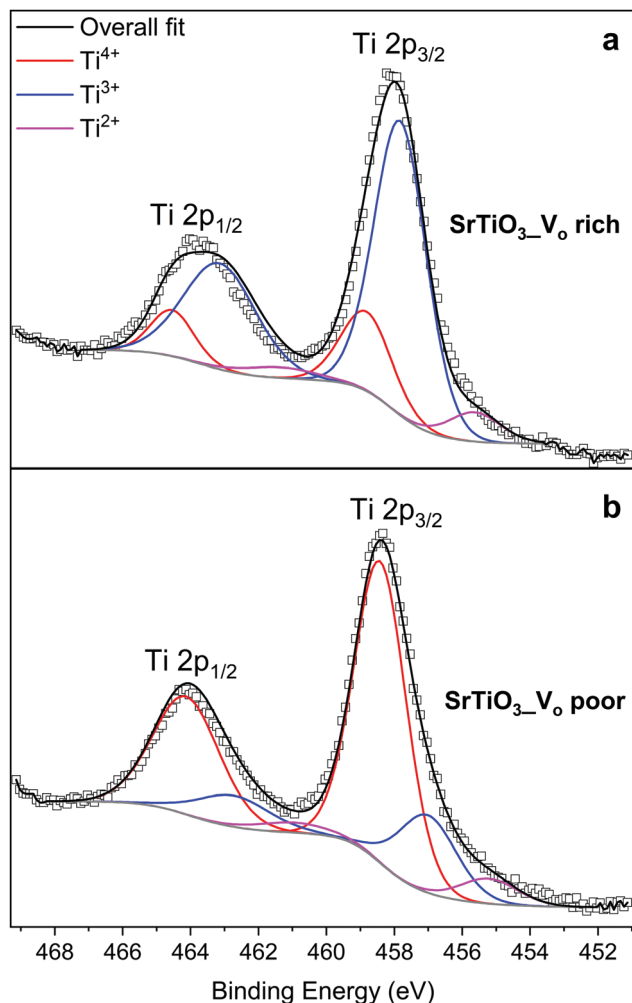


Fig. 8 XPS spectra of the Ti 2p region: (a) V_O rich $SrTiO_3$ made with heating profile 1 and (b) V_O poor $SrTiO_3$ made with heating profile 2.

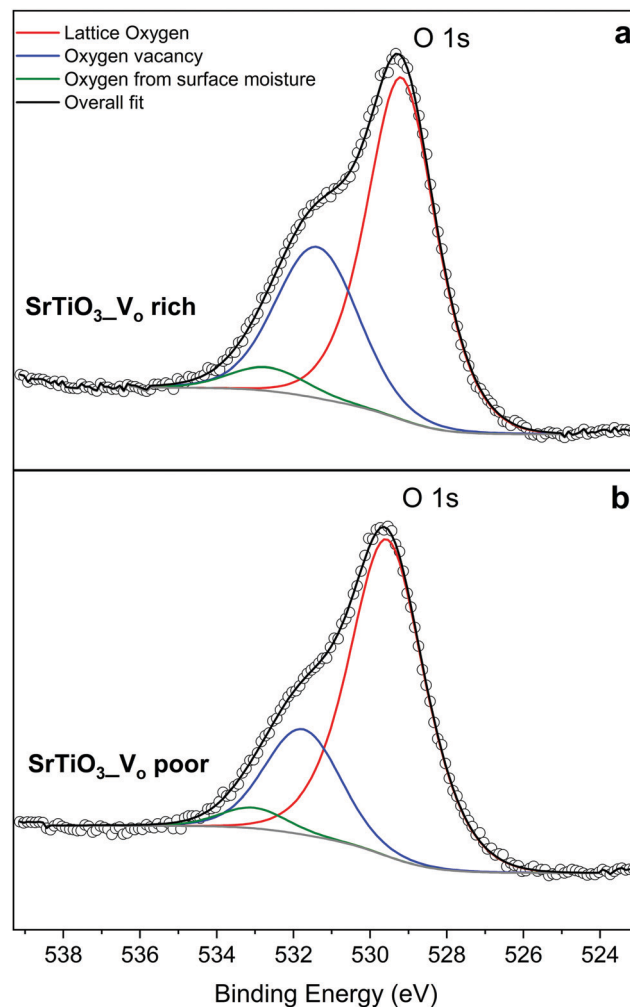


Fig. 9 XPS data of the oxygen species in (a) V_O rich $SrTiO_3$ made with heating profile 1 and (b) V_O poor $SrTiO_3$ made with heating profile 2.

and poor $SrTiO_3$ suggests that the malonic acid–choline chloride DES provides a reducing atmosphere during the calcination of doped or undoped $SrTiO_3$ samples. The prolonged heating of a sample in this reducing atmosphere leads to the increased amount of Ti^{3+} in the V_O rich samples made with heating profile 1. The XPS spectra in the Sr 3d region are similar for $SrTiO_3$ prepared by both heating methods, suggesting that Sr is in +2 oxidation state, irrespective of the heating profile used (Fig. S4, ESI†).

The O 1s spectra shown in Fig. 9 can also be fitted with 3 peaks. Fig. 9(a) represents the O 1s spectra of V_O rich $SrTiO_3$. The peak in red at 529.0 eV^{22,52} corresponds to the lattice oxygen in the crystal structure of $SrTiO_3$, the blue peak at 531.2 eV⁵² suggests the oxygen vacancies within the synthesized sample, and the green peak at 532.5⁵⁵ likely corresponds to loosely bound oxygen species at the sample due to atmospheric moisture. The O 1s spectra of V_O poor $SrTiO_3$ shown in Fig. 9(b) are shifted to higher binding energies by 0.6 eV. The fitted peak with the red line observed at 529.6 eV is attributed to the lattice oxygen, the fitted peak with the blue line at 531.8 eV corresponds to the oxygen vacancy and the fitted peak in green at

533.1 eV corresponds to the loosely bound oxygen from surface moisture. The amount of oxygen vacancy in the V_O rich $SrTiO_3$ sample was deduced from the fitted peaks in blue to be 32.4% while the V_O poor $SrTiO_3$ sample had 23.6% oxygen vacancy. The larger quantity of oxygen vacancies in V_O rich $SrTiO_3$ made with heating profile 1 can also explain its smaller unit cell parameter (Fig. 4). V_O rich $SrTiO_3$ has a unit cell parameter of 3.9050(4) Å which is 0.003 Å smaller than the unit cell parameter of V_O poor $SrTiO_3$. The same trend is seen for Al-doped $SrTiO_3$ prepared *via* two heating profiles with V_O rich Al-doped $SrTiO_3$ having overall smaller unit cell parameter compared to V_O poor Al-doped $SrTiO_3$ (Fig. 4). It should be noted that an atomic vacancy cannot be directly measured by the XPS, so the peaks assigned to the oxygen vacancy actually correspond to oxygen atoms near the vacant site. The survey spectra (Fig. S5, ESI†) suggest the absence of any other impurity element except the expected surface carbon, albeit the detection limit of XPS is 0.1–1 at%. It should also be noted that XPS is a surface technique and the percent of Ti^{3+} /oxygen vacancies is not representative of the bulk sample.



Photocatalytic activity

The photocatalytic activity of SrTiO_3 for overall water splitting under UV illumination was investigated after loading a $\text{Rh}_x\text{Cr}_{2-x}\text{O}_3$ proton reduction cocatalyst (for details see experimental section). As can be seen from Fig. 10 and Fig. S6 (ESI[†]), all samples evolve only small amounts of H_2 and only trace amounts of O_2 can be detected, likely from residual dissolved oxygen in the reaction mixtures. This suggests that H_2 evolution is stoichiometric, not catalytic, and the SrTiO_3 samples themselves serve as the electron source for the evolved H_2 . We find that V_O poor SrTiO_3 showed a higher H_2 evolution rate than that of the V_O rich SrTiO_3 . This suggests that photocatalytic H_2 evolution activity and $\text{V}_\text{O}/\text{Ti}^{3+}$ are inversely correlated. The H_2 amounts also varied with Al^{3+} content, although no activity

increase or trend could be seen. These findings are in contrast with previous observations of strong water splitting activity with micro- and nanosized Al-doped SrTiO_3 made by flux or hydrothermal syntheses.^{22–25,56} Those samples had mostly cubic morphology and well-defined facets which promoted carrier separation. The necessity for a well-faceted highly crystalline photocatalyst was further emphasized in the recent work by Takata *et al.*²⁵ It was reported that oxygen evolution reaction preferably occurred on the (110) facets while hydrogen evolution reactions occurred on the (100) facets. As previously reported by Zhao *et al.*,²² the Ti^{3+} sites act as recombination sites for photogenerated holes and electrons which leads to a reduction in the photocatalytic activity of SrTiO_3 . We therefore hypothesize that the absence of water splitting activity in the DES-synthesized materials is a result of both the absence of a faceted morphology, as well as the presence of a substantial amount of Ti^{3+} recombination sites. This hypothesis is supported by separate H_2 evolution experiments on Pt-modified V_O rich SrTiO_3 and Al- SrTiO_3 samples in aqueous methanol (Fig. S7, ESI[†]). Again, only low H_2 amounts are formed with external quantum efficiencies (EQE) of 0.017% and 0.0121% (both at 375 nm) for Pt/ SrTiO_3 and Pt/ $\text{SrTi}_{0.9}\text{Al}_{0.1}\text{O}_3$, respectively. These reactions use methanol as an easy-to oxidize sacrificial electron donor and Pt as an efficient proton reduction co-catalyst. The low EQE values confirm that the low photocatalytic activity is intrinsic to the DES-synthesized materials.

To study the photochemical charge separation ability of V_O rich and poor SrTiO_3 and $\text{SrTi}_{0.9}\text{Al}_{0.1}\text{O}_3$, surface photovoltage (SPV) spectroscopy was conducted on particle films on FTO (Fig. 11). Here, a vibrating gold probe measures the contact potential difference (CPD) of the sample. The CPD value in the dark is given by the Fermi level difference between the gold probe and the sample, while the change (ΔCPD) under illumination equals the surface photovoltage.^{57,58} The SPV spectrum for V_O rich Al³⁺-doped SrTiO_3 in Fig. 11(a) shows an SPV onset at 2.63 eV and a maximum SPV signal at 3.6 eV. From the tangent of this major signal, the effective band gap of 3.09 eV can be extracted. This value is in good agreement with the optical bandgap in Fig. 7. Hence, the major photovoltage signal is attributed to band gap excitation of Al³⁺-doped SrTiO_3 and charge transfer as shown in Fig. 12. The spectrum for the V_O rich Al³⁺-free SrTiO_3 is also shown in Fig. 11(a). Here, the photovoltage signal starts at 1.8 eV and the effective bandgap appears at 2.63 eV. These low energy features are attributed to excitation of Ti^{3+} mid-gap states as shown in Fig. 12, and hole trapping in SrTiO_3 surface states. Based on the SPV spectroscopy data, the Ti^{3+} mid-gap state's concentration in V_O rich Al³⁺-doped SrTiO_3 is greatly reduced. This confirms that Al³⁺ doping eliminates Ti^{3+} states for the V_O rich samples obtained via heating profile 1.

SPV spectra for the V_O poor samples are shown in Fig. 11(b). Again, the photovoltage maximum is seen at 3.6 eV, but this time the photovoltage onset and the effective band gaps of both samples occur much earlier (2.05–2.18 eV). This suggests that V_O poor undoped and Al-doped SrTiO_3 have higher mid-bandgap defect concentrations than V_O rich samples. Also, this

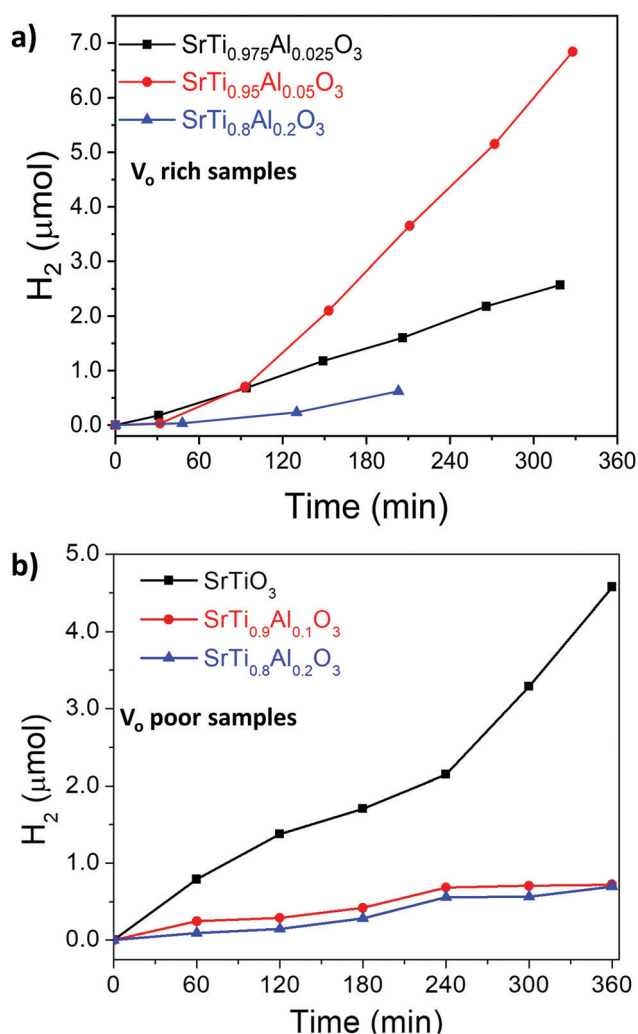


Fig. 10 Hydrogen evolution of (a) V_O rich samples made with heating profile 1 and (b) V_O poor samples made with heating profile 2 from water. Conditions: 100 mW cm^{-2} UV light from Xe-arc lamp, 100 mg $\text{Rh}_x\text{Cr}_{2-x}\text{O}_3/\text{SrTiO}_3$ (or $\text{Rh}_x\text{Cr}_{2-x}\text{O}_3/\text{SrTiO}_3:\text{Al}$) powder in 100 mL water. Oxygen was also detected for V_O rich samples made with heating 1 (see also Fig. S6, ESI[†]), while no oxygen was detected for V_O poor samples made with heating 2.



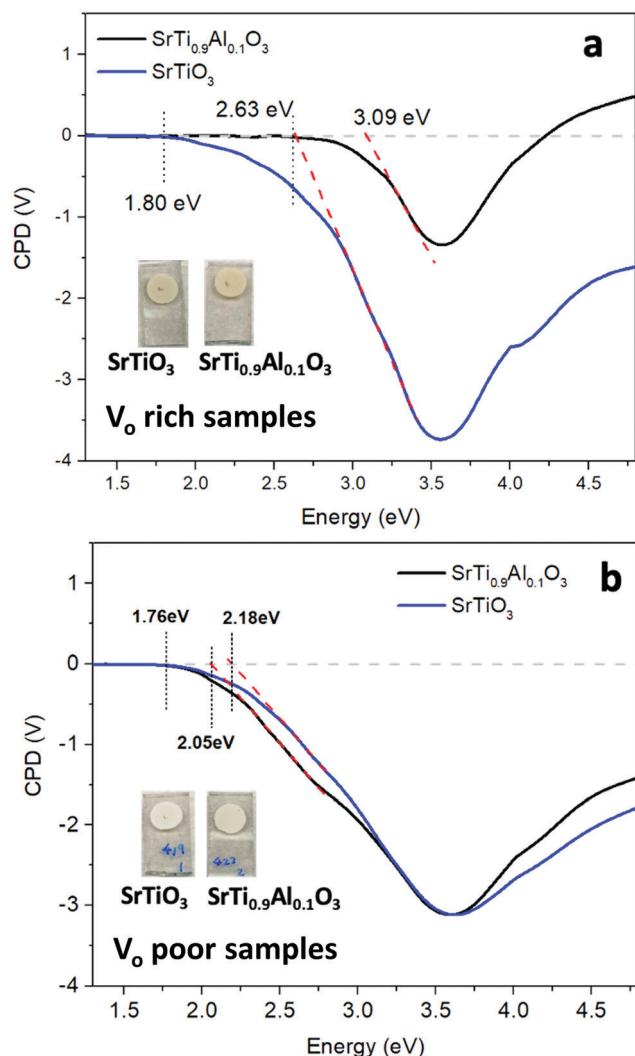


Fig. 11 Surface photovoltage (SPV) spectra of SrTiO_3 (blue) and $\text{SrTi}_{0.9}\text{Al}_{0.1}\text{O}_3$ (black) (a) V_O rich made by heating profile 1 and (b) V_O poor made by heating profile 2, respectively. CPD values under illumination are reported relative to the dark. The band-like onset was approximated by linear extrapolation (red dash). The inset pictures show the appearance of the respective films used for SPV measurement.

time, Al^{3+} doping does not eliminate the sub-bandgap signal, suggesting that the defects are not from Ti^{3+} . This suggests that V_O poor Al-doped and undoped SrTiO_3 contain additional impurities, likely at their surface. As shown in the SEM images (Fig. 5(a), (b) and Fig. S1a, b, ESI[†]), fast heating profile 2 produces V_O poor SrTiO_3 with more irregular particle morphology, which may be correlated with structural defects or the unintentional doping of a minute amount of carbon, nitrogen or chlorine arising from trapping of volatiles or incomplete burn-off of the organic eutectic. It should be noted that SPV band gaps are often smaller than optical band gaps because SPV is more sensitive to states in the forbidden region near the band edges. Additionally, the sensitivity of SPV measurement to the impurity elements is higher than that of XPS.⁵⁹

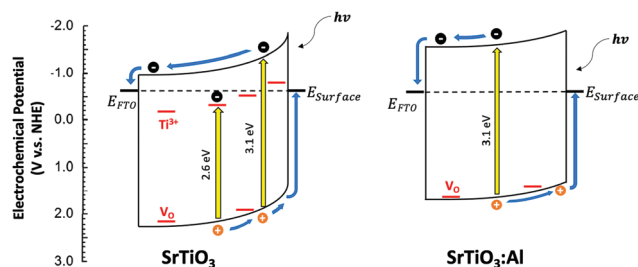


Fig. 12 Charge transfer and energetics during the SPV experiment for V_O rich SrTiO_3 and Al-doped SrTiO_3 (heating 1). In $\text{SrTiO}_3\text{:Al}$, Ti^{3+} trap states were eliminated by Al^{3+} doping, leading to a less reducing Fermi level, fewer trapped electrons, and less band bending. The lower band bending in $\text{SrTiO}_3\text{:Al}$ is indicated by the lesser surface photovoltage signal. E_Surface denotes the energy of surface states resulting from dangling bonds, reduced ions, or surface adsorbates. Ti^{3+} and V_O lattice defects (shown in red) are responsible for the sub-band gap photovoltage signal. E_FTO is the Fermi level of the fluorine doped tin oxide substrate.

Conclusions

SrTiO_3 and Al-doped SrTiO_3 were synthesized using a deep eutectic solvent consisting of a choline chloride and malonic acid mixture; the properties of the synthesized samples were investigated without any post-synthesis treatment. Titanium(IV) oxide bis(2,4-pentanedionate) employed in the synthesis as a titanium precursor is a stable powder which is easy to handle and dissolve in a choline chloride–malonic acid DES.²⁷ Al solid-state NMR showed that Al^{3+} was indeed doped into the symmetric octahedral Ti^{4+} site and also revealed the presence of an amorphous alumina impurity which was not detected by PXRD. The unit cell size, oxygen deficiency, Al-doping fraction and bandgap were tuned by variation in heating profile. Samples made with longer dwelling time and slower ramping (heating profile 1) had more of TiO_2 impurity and bigger crystallite sizes. Perovskite SrTiO_3 prepared *via* longer heating exhibits higher concentration of oxygen vacancies (V_O rich) and Ti^{3+} species, resulting in darker beige color, smaller bandgap and a smaller unit cell size. Samples made with shorter dwelling times and faster ramping rate (heating profile 2) are characterized by higher purity and smaller crystallite sizes. Strontium titanate prepared *via* this method has lower concentration of Ti^{3+} /oxygen vacancies (V_O poor), resulting in lighter beige color, wider bandgap, and larger cubic unit cell volume. Surface photovoltage spectroscopy confirms that Al^{3+} dopants can eliminate Ti^{3+} defects in Al-doped SrTiO_3 (heating 1), but that Al^{3+} doping has no effect on the defects in SrTiO_3 (heating 2). The latter defects might be a result of unintentional doping of trace amount of carbon, nitrogen or chlorine from the DES which are below the detection of X-ray photoelectron spectroscopy. The defects and the lack of clear facets are reasons for the lack of photocatalytic activity of the synthesized materials for water splitting or hydrogen evolution from aqueous methanol.

Conflicts of interest

There are no conflicts to declare.

Acknowledgements

Financial support for J. V. Z. in the form of start-up funds from Iowa State University is gratefully acknowledged. ²⁷Al solid-state NMR experiments and data analysis (A. V. and A. J. R.) were supported by the U.S. Department of Energy (DOE), Office of Science, Basic Energy Sciences, Materials Science and Engineering Division. The Ames Laboratory is operated for the U.S. DOE by Iowa State University under Contract DE-AC02-07CH11358. We thank Dr Kirill Kovnir (Department of Chemistry, Iowa State University and Ames Laboratory) for the access to the PXRD diffractometer; Dr Javier Vela (Department of Chemistry, Iowa State University and Ames Laboratory) for the access to the UV-vis spectrometer; Dr Warren Straszheim (Materials Analysis Research Laboratory, Iowa State University) and Aishwarya Mantravadi (Iowa State University) for the help with SEM/EDS data acquisition. The photocatalytic and the surface photovoltage spectroscopy results are based upon work supported by the U.S. Department of Energy, Office of Science, Office of Basic Energy Sciences, under Award Number DE-SC0015329.

References

- 1 A. P. Abbott, G. Capper, D. L. Davies, R. K. Rasheed and V. Tambyrajah, *Chem. Commun.*, 2003, 70–71.
- 2 A. P. Abbott, D. Boothby, G. Capper, D. L. Davies and R. K. Rasheed, *J. Am. Chem. Soc.*, 2004, **126**, 9142–9147.
- 3 A. P. Abbott, G. Capper, D. L. Davies, K. J. McKenzie and S. U. Obi, *J. Chem. Eng. Data*, 2006, **51**, 1280–1282.
- 4 Q. H. Zhang, K. D. Vigier, S. Royer and F. Jerome, *Chem. Soc. Rev.*, 2012, **41**, 7108–7146.
- 5 X. Ge, C. D. Gu, X. L. Wang and J. P. Tu, *J. Mater. Chem. A*, 2017, **5**, 8209–8229.
- 6 A. Soldner, J. Zach, M. Iwanow, T. Gartner, M. Schlosser, A. Pfitzner and B. Konig, *Chem. – Eur. J.*, 2016, **22**, 13108–13113.
- 7 S. Hong, R. M. Doughty, F. E. Osterloh and J. V. Zaikina, *J. Mater. Chem. A*, 2019, **7**, 12303–12316.
- 8 S. Hong, S. J. Burkhov, R. M. Doughty, Y. Cheng, B. J. Ryan, A. Mantravadi, L. T. Roling, M. G. Panthani, F. E. Osterloh, E. A. Smith and J. V. Zaikina, *Chem. Mater.*, 2021, **33**(5), 1667–1682.
- 9 R. Boston, P. Y. Foeller, D. C. Sinclair and I. M. Reaney, *Inorg. Chem.*, 2017, **56**, 542–547.
- 10 R. C. Neville, C. A. Mead and B. Hoeneise, *J. Appl. Phys.*, 1972, **43**, 2124.
- 11 A. Tkach, O. Okhay, P. M. Vilarinho and A. L. Kholkin, *J. Phys.: Condens. Matter*, 2008, **20**, 415224.
- 12 J. Qi, M. Cao, J. P. Heath, J. S. Dean, H. Hao, Z. Yao, Z. Yu and H. Liu, *J. Mater. Chem. C*, 2018, **6**, 9130–9139.
- 13 J. B. Li, J. Wang, J. F. Li, Y. Li, H. Yang, H. Y. Yu, X. B. Ma, X. B. Yaer, L. Liu and L. Miao, *J. Mater. Chem. C*, 2018, **6**, 7594–7603.
- 14 A. I. Abutaha, S. R.-S. Kumar, A. M. Dehkordi, T. M. Tritt and H. N. Alshareef, *J. Mater. Chem. C*, 2014, **2**, 9712–9719.
- 15 K. van Benthem, C. Elsasser and R. H. French, *J. Appl. Phys.*, 2001, **90**, 6156–6164.
- 16 T. Tomio, H. Miki, H. Tabata, T. Kawai and S. Kawai, *J. Appl. Phys.*, 1994, **76**, 5886–5890.
- 17 B. L. Phoon, C. W. Lai, J. C. Juan, P.-L. Show and G.-T. Pan, *Int. J. Hydrogen Energy*, 2019, **44**, 14316–14340.
- 18 A. Frye, R. H. French and D. A. Bonnell, *Z. Metallkd.*, 2003, **94**, 226–232.
- 19 J. G. Mavroides, J. A. Kafalas and D. F. Kolesar, *Appl. Phys. Lett.*, 1976, **28**, 241–243.
- 20 K. Domen, S. Naito, M. Soma, T. Onishi and K. Tamaru, *J. Chem. Soc., Chem. Commun.*, 1980, 543–544.
- 21 T. Takata and K. Domen, *J. Phys. Chem. C*, 2009, **113**, 19386–19388.
- 22 Z. Q. Zhao, R. V. Goncalves, S. K. Barman, E. J. Willard, E. Byle, R. Perry, Z. K. Wu, M. N. Huda, A. J. Moule and F. E. Osterloh, *Energy Environ. Sci.*, 2019, **12**, 1385–1395.
- 23 Y. Ham, T. Hisatomi, Y. Goto, Y. Moriya, Y. Sakata, A. Yamakata, J. Kubota and K. Domen, *J. Mater. Chem. A*, 2016, **4**, 3027–3033.
- 24 Z. Q. Zhao, E. J. Willard, H. Li, Z. K. Wu, R. H.-R. Castro and F. E. Osterloh, *J. Mater. Chem. A*, 2018, **6**, 16170–16176.
- 25 T. Takata, J. Z. Jiang, Y. Sakata, M. Nakabayashi, N. Shibata, V. Nandal, K. Seki, T. Hisatomi and K. Domen, *Nature*, 2020, **581**, 411–414.
- 26 R. Konta, T. Ishii, H. Kato and A. Kudo, *J. Phys. Chem. B*, 2004, **108**, 8992–8995.
- 27 J. S. Wang, S. Yin, M. Komatsu, Q. W. Zhang, F. Saito and T. Sato, *Appl. Catal., B*, 2004, **52**, 11–21.
- 28 E. Rocha-Rangel, J. Lopez-Hernandez, J. A. Rodriguez-Garcia, E. N. Armendariz-Mireles, C. A. Calles-Arriaga, W. J. Pech-Rodriguez and J. A. Castillo-Robles, *J. Ceram. Process. Res.*, 2017, **18**, 590–593.
- 29 Y. Z. Fan, Z. Y. Zhou, Y. Chen, W. Huang and X. L. Dong, *J. Mater. Chem. C*, 2020, **8**, 50–57.
- 30 Y. Yamaguchi, Y. Kanamaru, M. Fukushima, K. Fujimoto and S. Ito, *J. Am. Ceram. Soc.*, 2015, **98**, 3054–3061.
- 31 Y. Ma, Z. J. Wu, H. W. Wang, G. Q. Wang, Y. K. Zhang, P. C. Hu, Y. M. Li, D. K. Gao, H. Q. Pu, B. Z. Wang and X. W. Qi, *CrystEngComm*, 2019, **21**, 3982–3992.
- 32 Z. R. Wang, X. C. Ren, C. W. Leung, S. Q. Shi and P. K.-L. Chan, *J. Mater. Chem. C*, 2013, **1**, 3825–3832.
- 33 G. Pfaff, *J. Mater. Chem.*, 1993, **3**, 721–724.
- 34 L. H. Hu, C. D. Wang, R. M. Kennedy, L. D. Marks and K. R. Poeppelmeier, *Inorg. Chem.*, 2015, **54**, 740–745.
- 35 L. A. Crosby, B. R. Chen, R. M. Kennedy, J. G. Wen, K. R. Poeppelmeier, M. J. Bedzyk and L. D. Marks, *Chem. Mater.*, 2018, **30**, 841–846.
- 36 T. K. Townsend, N. D. Browning and F. E. Osterloh, *ACS Nano*, 2012, **6**, 7420–7426.
- 37 *PDXL: Integrated X-ray powder diffraction software, Version 2.8.1.1*, Rigaku, 2018.
- 38 V. Petricek, M. Dusek and L. Palatinus, *Z. Kristallogr.*, 2014, **229**(5), 345–352.
- 39 A. Samoson and E. Lippmaa, *Phys. Rev. B: Condens. Matter Mater. Phys.*, 1983, **28**, 6567–6570.
- 40 E. Lippmaa, A. Samoson and M. Magi, *J. Am. Chem. Soc.*, 1986, **108**, 1730–1735.
- 41 J.-B. d'Espinose de la Caillerie, C. Fretigny and D. Massiot, *J. Magn. Reson.*, 2008, **192**, 244–251.



- 42 S. G.-J. van Meerten, W. M.-J. Franssen and A. P.-M. Kentgens, *J. Magn. Reson.*, 2019, **301**, 56–66.
- 43 R. M. Doughty, F. A. Chowdhury, Z. Mi and F. E. Osterloh, *J. Chem. Phys.*, 2020, **153**, 144707.
- 44 K. Maeda, K. Teramura, H. Masuda, T. Takata, N. Saito, Y. Inoue and K. Domen, *J. Phys. Chem. B*, 2006, **110**, 13107–13112.
- 45 F. Wang, Q. Xu, Z.-a Tan, D. Qian, Y. Ding, L. Li, S. Li and Y. Li, *Org. Electron.*, 2012, **13**, 2429–2435.
- 46 S. F. Dec, M. F. Davis, G. E. Maciel, C. E. Bronnimann, J. J. Fitzgerald and S. S. Han, *Inorg. Chem.*, 1993, **32**, 955–959.
- 47 A. Faucher, V. V. Terskikh, E. Ye, G. M. Bernard and R. E. Wasylshen, *J. Phys. Chem. A*, 2015, **119**, 11847–11861.
- 48 I. Bykov, M. Makarova, V. Trepakov, A. Dejneka, L. Yurchenko, A. Jaeger and L. Jastrabik, *Phys. Status Solidi B*, 2013, **250**, 821–824.
- 49 C. Gervais, D. Veautier, M. E. Smith, F. Babonneau, P. Belleville and C. Sanchez, *Solid State Nucl. Magn. Reson.*, 2004, **26**, 147–152.
- 50 L. Samain, A. Jaworski, M. Eden, D. M. Ladd, D. K. Seo, F. J. Garcia-Garcia and U. Haussermann, *J. Solid State Chem.*, 2014, **217**, 1–8.
- 51 C. V. Chandran, C. E.-A. Kirschhock, S. Radhakrishnan, F. Taulelle, J. A. Martens and E. Breynaert, *Chem. Soc. Rev.*, 2019, **48**, 134–156.
- 52 H. Q. Tan, Z. Zhao, W. B. Zhu, E. N. Coker, B. S. Li, M. Zheng, W. X. Yu, H. Y. Fan and Z. C. Sun, *ACS Appl. Mater. Interfaces*, 2014, **6**, 19184–19190.
- 53 W. L. Zhao, W. Zhao, G. L. Zhu, T. Q. Lin, F. F. Xu and F. Q. Huang, *CrystEngComm*, 2015, **17**, 7528–7534.
- 54 M. C. Biesinger, L. W.-M. Lau, A. R. Gerson and R. S.-C. Smart, *Appl. Surf. Sci.*, 2010, **257**, 887–898.
- 55 M. C. Biesinger, B. P. Payne, L. W.-M. Lau, A. Gerson and R. S.-C. Smart, *Surf. Interface Anal.*, 2009, **41**, 324–332.
- 56 M. Klusackova, R. Nebel, K. M. Macounova, M. Klementova and P. Krtil, *Electrochim. Acta*, 2019, **297**, 215–222.
- 57 T. Dittrich and S. Fengler, *Surface Photovoltage Analysis of Photoactive Materials*, World Scientific Publishing Europe Ltd., London, 2020, p. 287.
- 58 J. Zhao and F. E. Osterloh, *J. Phys. Chem. Lett.*, 2014, **5**, 782–786.
- 59 J. Lagowski, P. Edelman, A. M. Kontkiewicz, O. Milic, W. Henley, M. Dexter, L. Jastrzebski and A. M. Hoff, *Appl. Phys. Lett.*, 1993, **63**, 3043–3045.

